Topological edge and corner states in the biphenylene network

Keiki Koizumi,[1] Huyen Thanh Phan,[1] Kento Nishigomi,[1] and Katsunori Wakabayashi[1,2,3]
[1]*Department of Nanotechnology for Sustainable Energy, School of Science and Technology, Kwansei Gakuin University, Gakuen-Uegahara 1, Sanda 669-1330, Japan*
[2]*National Institute for Materials Science, Namiki 1-1, Tsukuba 305-0044, Japan*
[3]*Center for Spintronics Research Network, Osaka University, Toyonaka 560-8531, Japan*

(Received 3 November 2023; accepted 3 January 2024; published 25 January 2024)

The electronic states and topological properties of the biphenylene network (BPN) are analyzed using a tight-binding model based on the π-electron network. It is shown that tuning the hopping parameters induces topological phase transitions, leading to the emergence of edge states owing to the nontrivial topological Zak phase of the bulk BPN. Elementary band analysis clearly gives the number of edge states, which are associated with the location of Wannier centers. In addition, we present the conditions for the emergence of corner states owing to the higher-order topological nature of the BPN.

DOI: 10.1103/PhysRevB.109.035431

I. INTRODUCTION

The concept of topology has brought about a paradigm shift in modern condensed matter physics, opening up the research field of topological materials. These materials include topological insulators [1–10], topological crystalline insulators [11–13], topological semimetals [14–19], and so on. One of the essential properties of topologically nontrivial systems is the bulk-edge correspondence, where robust edge and surface states appear at the interfaces that separate two topologically distinct systems. These topologically protected states are insensitive to local perturbation such as edge roughness and disorder, which may serve for the application to ultralow-power-consumption electronics and quantum computation. The idea of device design based on topology was also recently applied to photonics [20–23] and other systems [24,25].

In a system with both time reversal and crystal inversion symmetries, the Zak phase can serve as a good topological invariant for characterizing the bulk-edge correspondence [26]. Since the Zak phase is associated with charge polarization [27–31], a nontrivial finite Zak phase predicts the presence of edge-localized states when an edge is introduced to the system. In graphene, a one-atom-thick two-dimensional (2D) carbon sheet, the edges induce the electron localized states (edge states) at the Fermi energy [32–34]. However, the edge states crucially depend on the shape of the edges and are absent for armchair edges. This puzzle can be resolved by considering the Zak phase of the bulk wave function of graphene, which gives the momentum-dependent Zak phase [35,36]. The Zak phase is identically zero solely for the armchair edge, i.e., no edge states, which is consistent with various numerical calculations [37,38]. The presence of edge states provides the spin polarization [32,39] and a perfectly conducting channel [40].

Recently, the biphenylene network (BPN), a newly synthesized 2D sp^2-carbon-based material, was successfully synthesized by Fan *et al.* [41]. The BPN has a fascinating lattice structure, where the hexagonal carbon rings are organized on a square lattice, resulting in a 2D tiling pattern that includes four-, six-, and eight-member rings. Previous studies reported thermal conductivity, magnetic properties, and hydrogen storage properties based on first-principles calculations [42–45]. Also, Ref. [44] reported Zak phases and topological grain boundary states along BPN nanoribbons. However, the higher-order topological corner states have not been considered yet. Here, we also employ elementary band analysis, which clearly gives the number of edge states, which are associated with the locations of Wannier centers.

In this paper, we theoretically study the electronic and topological properties of the 2D BPN. Since the BPN comprises only sp^2 carbon atoms similar to graphene, the π electrons govern the electronic states of the BPN near the Fermi energy. Thus, we employ the tight-biding model, which describes π-electronic states of the 2D BPN to analyze the topological properties. We will demonstrate that successive topological phase transitions occur by tuning the ratio between intra- and intercellular electron hoppings. In the Su-Schrieffer-Heeger (SSH) model [46,47], a similar topological phase transition can occur, inducing a nontrivial Zak phase, resulting in the edge states [36,48–50]. We also find that the topological properties of the BPN are characterized by the Zak phase of the bulk wave function. Charge polarization at the surfaces, i.e., edge states, is induced if the Zak phase possesses π. By studying BPN nanoribbons, we attribute the appearance of edge states to the Zak phase of π. Furthermore, we demonstrate that the exact number of edge states can be determined by considering the position of the Wannier orbital. Similar arguments can be used to show the existence of topological corner states.

This paper is organized as follows. In Sec. II, we investigate the electronic states of π electrons of the BPN using a tight-binding model. Considering two types of hopping energies, we show that the topological phase transition occurs at a specific ratio. In Sec. III, we illustrate the existence of the edge states in the BPN guaranteed by the nontrivial Zak phase and the central position of the Wannier function. In addition, we find multiple corner states in the BPN nanoflake. Section IV provides a summary of the paper.

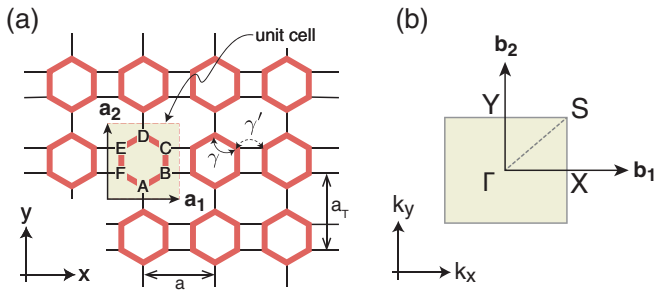

FIG. 1. (a) The lattice structure of the BPN. The shaded region is the unit cell, with six nonequivalent sublattices of carbon atoms (A to F). $\boldsymbol{a}_1 = (a, 0)$ and $\boldsymbol{a}_2 = (0, a_T)$ are two primitive vectors, where a and $a_T = \frac{3a}{\sqrt{3}+1}$. The intracellular (intercellular) hoppings denoted by red (black) lines are γ (γ'). (b) The first BZ of the BPN and its high-symmetry points, $\Gamma = (0, 0)$, $X = (\pi/a, 0)$, $Y = (0, \pi/a_T)$, and $S = (\pi/a, \pi/a_T)$.

II. ELECTRONIC STATES OF THE 2D BPN

A. Tight-binding model

Figure 1(a) displays the schematic of the lattice structure for the 2D BPN, where the hexagonal carbon rings are organized on a square lattice, resulting in a 2D tiling pattern that includes four-, six-, and eight-member rings. The shaded rectangle in Fig. 1(a) represents the unit cell. Since the BPN is composed of sp^2 carbon atoms, the electronic states of the 2D BPN near the Fermi energy are governed by π electrons. Now let us consider the nearest-neighbor tight-binding model for π electrons of the 2D BPN. The BPN contains six geometrically nonequivalent carbon atoms (A, B, C, D, E, and F) in the unit cell, as shown in Fig. 1(a). Here, $\boldsymbol{a}_1 = (a, 0)$ and $\boldsymbol{a}_2 = (0, a_T)$ are the primitive vectors. a and $a_T = \frac{3a}{\sqrt{3}+1}$ are lattice periodicities along the x and y directions, respectively. The length of a is 3.7554 Å. We shall introduce two kinds of electron hoppings: γ is the intracellular hopping, and γ' is the intercellular hopping. Figure 1(b) shows the first Brillouin zone (BZ) with high-symmetry points, i.e., $\Gamma = (0, 0)$, $X = (\frac{\pi}{a}, 0)$, $Y = (0, \frac{\pi}{a_T})$, and $S = (\frac{\pi}{a}, \frac{\pi}{a_T})$. The actual parameter set to reproduce the energy band structure for π electrons of the 2D BPN is given in the Appendix.

The eigenvalue equation of the 2D BPN is described as

$$\hat{H}(\boldsymbol{k})\,|u_{n,\boldsymbol{k}}\rangle = E_{n,\boldsymbol{k}}\,|u_{n,\boldsymbol{k}}\rangle\,, \tag{1}$$

where $\hat{H}(\boldsymbol{k})$ is the Hamiltonian at wave number $\boldsymbol{k} = (k_x, k_y)$ and $E_{n,\boldsymbol{k}}$ is the eigenvalue with band index n ($= 1, 2, \ldots, 6$). The eigenvector $|u_{n,\boldsymbol{k}}\rangle$ is written as

$$|u_{n,\boldsymbol{k}}\rangle = [c_{n,A}(\boldsymbol{k}), c_{n,B}(\boldsymbol{k}), c_{n,C}(\boldsymbol{k}), c_{n,D}(\boldsymbol{k}), c_{n,E}(\boldsymbol{k}), c_{n,F}(\boldsymbol{k})]^T,$$

where $[\cdots]^T$ means the transpose of the vector. $c_{n,\alpha}(\boldsymbol{k})$ is the amplitude of the wave function at site α for the nth band. The tight-binding Hamiltonian up to the nearest-neighbor hopping is

$$\hat{H}(\boldsymbol{k}) = -\gamma \begin{pmatrix} 0 & 1 & 0 & \rho_y & 0 & 1 \\ 1 & 0 & 1 & 0 & 0 & \rho_x^* \\ 0 & 1 & 0 & 1 & \rho_x^* & 0 \\ \rho_y^* & 0 & 1 & 0 & 1 & 0 \\ 0 & 0 & \rho_x & 1 & 0 & 1 \\ 1 & \rho_x & 0 & 0 & 1 & 0 \end{pmatrix}, \tag{2}$$

with

$$\rho_x = \frac{\gamma'}{\gamma} e^{i\boldsymbol{k}\cdot\boldsymbol{a}_1}, \quad \rho_y = \frac{\gamma'}{\gamma} e^{i\boldsymbol{k}\cdot\boldsymbol{a}_2}. \tag{3}$$

Figure 2(a) shows the energy band structure along the path connecting the high-symmetry points of the first BZ and the density of states (DOS) for $\gamma'/\gamma = 1$. Since the BPN has a π electron per atomic site on average, the Fermi energy is $E = 0$. There are six energy bands from the bottom to the top, and the corresponding band index is 1 to 6. The BPN is metallic with flat bands at $E = 0$. Also, owing to the crystal symmetry of the BPN, the energy dispersion has the following relation:

$$E_n(k_x, k_y) = -E_{6-(n-1)}\left(k_x \pm \frac{\pi}{a}, k_y\right). \tag{4}$$

Figure 2(b) is a three-dimensional plot of the energy band structure in the first BZ. It should be noted that the band touchings occur only on the Γ-X line. Figures 2(c) and 2(d) show the energy band structure on the Γ-X and Γ-Y lines,

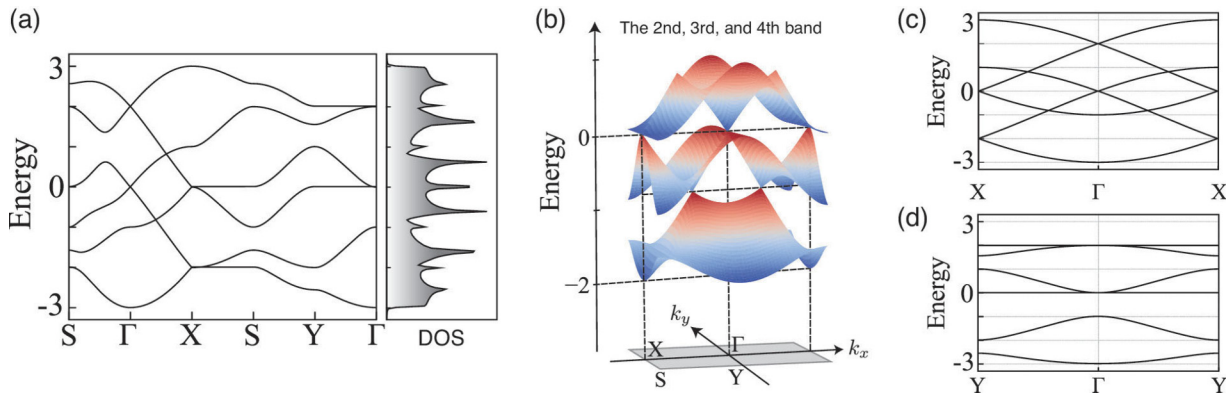

FIG. 2. (a) The energy band structure and the corresponding DOS for $\gamma'/\gamma = 1$. There are six subbands. (b) Three-dimensional plot of the energy band structure for bands 2, 3, and 4. (c) The energy band structure along the k_x direction. Tilted Dirac dispersions can be seen on the Γ-X line between bands 2 and 3. (d) The energy band structure along the k_y direction. Band 3 is flat along the Γ-Y line, and band 4 has a parabolic dispersion at the Γ point.

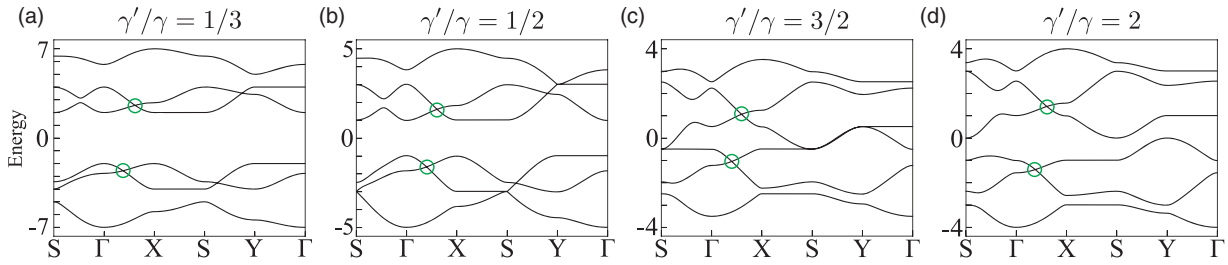

FIG. 3. Energy band structure of the 2D BPN for (a) $\gamma'/\gamma = 1/3$, (b) $\gamma'/\gamma = 1/2$, (c) $\gamma'/\gamma = 1.5$, and (d) $\gamma'/\gamma = 2$. The band degenerating points are marked with green circles.

respectively. The second and the third subbands linearly cross at a point on the Γ-X line, i.e., a tilted Dirac cone. Similarly, tilted Dirac cones also emerge between the fourth and fifth subbands. However, the third and fourth subbands touch differently at $E = 0$, i.e., isotropic energy dispersion. At the Γ point, these bands linearly touch along the k_x direction, whereas the third subband becomes flat and the fourth subband has a parabolic dispersion in the k_y direction. Additionally, at the X point, the third subband is parabolic along the X-S line, while the fourth subband is almost flat along the X-S line.

B. Effect of variable hopping energy

Figures 3(a)–3(d) show the energy band structures of the 2D BPN with several different ratios of hopping energy γ'/γ. It can be seen that the topology of the energy band structure crucially depends on the ratio of these two hopping parameters. In the BPN, the topological phase transition occurs at $\gamma'/\gamma = 1/2, 1$, and 1.5, where the band gap closes and reopens. The closing and reopening of the energy band gap cause a band inversion, resulting in a topological phase transition, i.e., a change in the value of the Zak phase.

In the range of $1/2 \leqslant \gamma'/\gamma \leqslant 1$, the first subband touches the second subband; similarly, the fifth subband touches the sixth subband. However, these band touchings are lifted for the other range and become isolated.

Furthermore, the third and fourth subbands touch at the Fermi energy in the range of $1 \leqslant \gamma'/\gamma \leqslant 1.5$. Therefore, a complete band gap opens when $\gamma'/\gamma < 1$ and $\gamma'/\gamma > 1.5$. There are four tilted Dirac cones on the Γ-X line; one is between the second and third subbands, and another one is between the fourth and fifth subbands. These crossing points are marked by green circles in Fig. 3. These four points are maintained in all cases.

III. TOPOLOGICAL PROPERTIES

A. Zak phase and topological edge states

We numerically calculate the Zak phase [26–31,36], which is given as the line integral of the Berry connection:

$$A_n(k_\parallel, k_\perp) = i \langle u_{n,\boldsymbol{k}} | \partial_{k_\perp} | u_{n,\boldsymbol{k}} \rangle . \tag{5}$$

The Berry connection physically means the vector potential in reciprocal space. In order to discuss the charge polarization based on the Zak phase, we have introduced two specific one-dimensional (1D) wave numbers, i.e., $k_\parallel$ and $k_\perp$. Here, $k_\parallel$ represents the 1D wave number parallel to the translational direction of the considered edge or ribbons. $k_\perp$ is a crystal momentum perpendicular to $k_\parallel$.

The Zak phase of the nth subband is defined as

$$Z_n(k_\parallel) = \int_C dk_\perp A_n(k_\parallel, k_\perp), \tag{6}$$

where C is a straight path along $k_\perp$ connecting two equivalent points of $\boldsymbol{k}$ in the 2D BZ. For an inversion-symmetric system, the Zak phase is quantized by 0 or π. Charge polarization for the nth subband P_n is related to the Zak phase as

$$P_n = \frac{1}{2\pi} Z_n. \tag{7}$$

Thus, if the nontrivial Zak phase of π appears, we obtain finite charge polarization at the surface or edge, which is nothing more than the edge states. Since the bulk topological properties are related to the charge polarization at the edges, this is referred to as bulk-edge correspondence. The Zak phase approach successfully predicts the topological edge states (TESs) for graphene, A3B nanosheets, the 2D SSH model, and so on [31,35,36,51].

Now, let us consider 1D biphenylene ribbons (BPRs). Figure 4 summarizes the lattice structure, electronic band structure, and Zak phase of BPRs. To discuss the electronic properties of BPRs, we shall define the translational vector of the BPR as $\boldsymbol{T} = m\boldsymbol{a_1} + n\boldsymbol{a_2} = T(m, n)$ and the corresponding reciprocal vector as $\boldsymbol{\Gamma}_\parallel = 2\pi \frac{\boldsymbol{T}}{|\boldsymbol{T}|^2}$. Figure 4(a) displays the schematic of a BPR with zigzag edges (zigzag BPR), where N is the width of the ribbons. Since the translational vector of a zigzag BPR is given as $\boldsymbol{T} = T(1, 0)$, the first BZ of a zigzag BPR is given as $|k_x| \leqslant \pi/a$, which is marked by thick magenta lines in Fig. 4(b). The integration path C for the calculation of the Zak phase is given by the cyan arrow in Fig. 4(b). The energy band structure for a zigzag BPR with $N = 50$ is shown in Fig. 4(c), where black lines indicate the modes of bulk states and cyan lines indicate the modes of topological edge states.

For a numerical calculation, we rewrite Eq. (6) as a discrete form using Taylor expansion up to first order, i.e.,

$$Z_n(k_\parallel) = -\mathrm{Im}\left[\ln\left(\prod_{j=1}^{N_0} \langle u_{n,\boldsymbol{k}_{\perp j}} | u_{n,\boldsymbol{k}_{\perp j+1}} \rangle \right) \right], \tag{8}$$

where $k_\parallel$ is a 1D momentum space parallel to $\boldsymbol{T}$. The integral path is divided into N_0 segments along $k_\perp$. Here, we impose for the wave function a gauge-fixing condition $|\langle \phi_g | u_{n,k_j} \rangle| \neq 0$ at all k_j points on the path with a global gauge ϕ_g, which is well defined in the whole BZ [52].

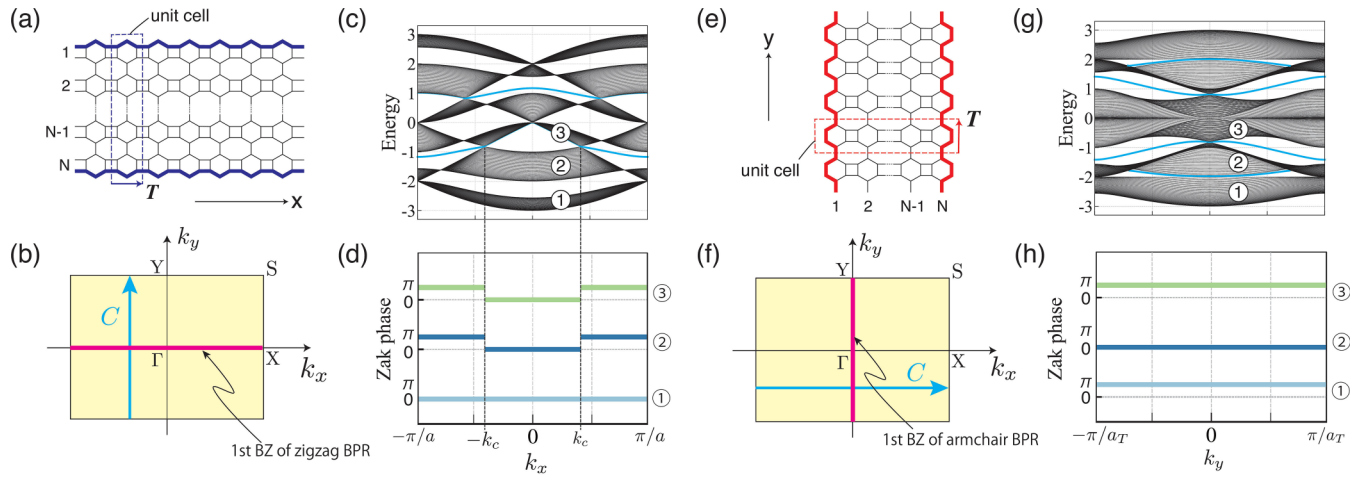

FIG. 4. (a) Schematic lattice structure of the BPN ribbon (BPR) with zigzag edges. N is the width of the ribbon. The translational vector $\boldsymbol{T}$ for the zigzag BPR is defined as $\boldsymbol{T} = T(1, 0)$. Here, $\boldsymbol{T} = m\boldsymbol{a}_1 + n\boldsymbol{a}_2 = T(m, n)$. (b) The first BZ of the zigzag BPR (thick magenta line). The shaded yellow area is the first BZ of the 2D BPN. In a zigzag BPR, its first BZ is projected onto the k_x axis and given as $-\pi/a \leqslant k_x \leqslant \pi/a$. The integration path C for the calculation of the Zak phase is taken along k_y. (c) Energy band structure for the zigzag BPR for $N = 50$. Cyan lines indicate the modes of TESs that emerge in the energy gaps where the total Zak phase is π. (d) The corresponding Zak phase of the zigzag BPR for the lowest three subbands, where the Zak phase is finite in the second and third subbands. (e) Schematic lattice structure of a BPR with armchair edges. N is the width of the ribbon. The translational vector $\boldsymbol{T}$ for the armchair BPR is defined as $\boldsymbol{T} = T(0, 1)$. (f) The first BZ of the zigzag BPR (thick magenta line). The shaded yellow area is the first BZ of the 2D BPN. In an armchair BPR, its first BZ is projected onto the k_y axis and given as $-\pi/a_T \leqslant k_y \leqslant \pi/a_T$. The integration path C for the calculation of the Zak phase is taken along k_x. (g) Energy band structure for the armchair BPR for $N = 50$. Cyan lines indicate the modes of TESs that emerge in the energy gaps where the total Zak phase is π. (h) The corresponding Zak phase for the armchair BPR for the lowest three subbands, where the Zak phase is finite in the first and the third subbands.

The emergence of TESs in zigzag BPRs can be associated with the nontrivial Zak phase of π. Figure 4(d) shows the k-dependent Zak phase of a zigzag BPR for the lowest three bands. The Zak phase of the first subband is always zero for any k, i.e., topologically trivial. However, in the second and third subbands, there are k regions ($|k| > k_c$) with a finite Zak phase of π, i.e., topologically nontrivial. Here, $\pm k_c$ are the positions of the Dirac point between the second and third subbands. Thus, the TESs emerge in the energy gap between the second and third subbands in the region of $|k| > k_c$ because $\sum_{n=1}^{2} Z_n(k) = \pi$ for $|k| < k_c$. However, since $\sum_{n=1}^{3} Z_n(k) = 0$ for any k, there is no TES in the energy gap between the third and fourth subbands. Other TESs above $E > 0$ are also explained in a similar manner.

Next, we shall analyze the electronic and topological properties of a BPR with armchair edges (armchair BPR). Figure 4(e) displays the schematic of an armchair BPR, where N is the width of the ribbon. The translational vector of armchair BPRs is given as $\boldsymbol{T} = (0, 1)$. Thus, the first BZ of armchair BPRs is given as $|k_y| \leqslant \pi/a_T$, which is marked by a thick cyan line in Fig. 4(f). The energy band structure of an armchair BPR with $N = 50$ is shown in Fig. 4(g), where the cyan lines in the energy gaps indicate TES modes.

The emergence of TES modes in armchair BPRs is also clearly explained by the analysis of the Zak phase. Figure 4(h) displays the k-dependent Zak phase for the lowest three subbands of the armchair BPR, which gives π, 0, and π from the lowest subband. Thus, the energy band gaps between the first and second subbands becomes topologically nontrivial because $Z_1(k) = \pi$. Similarly, the energy band gaps between the second and third subbands become topologically nontrivial because $\sum_{n=1}^{2} Z_n(k) = \pi$. These results are consistent with the emergence of TESs shown in Fig. 4(g). Other TESs above $E > 0$ are also explained similarly.

Similarly, from the viewpoint of the Zak phase, we illustrate the existence of TESs, even if we tune the ratio of the hopping energy, i.e., γ'/γ. Figures 5(a) and 5(b) display the energy band structures (top panels) and the corresponding Zak phases (bottom panels) for zigzag and armchair BPRs, respectively, with the ratio of hopping parameters tuned to $\gamma'/\gamma = 1/2$ and 2. For all cases of zigzag BPRs shown in Fig. 5(a), the emergence of TESs is consistent with the finite Zak phase of π. For armchair BPRs shown in Fig. 5(b), the emergence of TESs for $\gamma'/\gamma = 1/2$ (left panel) is consistent with the presence of the nontrivial Zak phase of π. For $\gamma'/\gamma = 2$ (right panel), the emergence of two TES modes shown by magenta lines in the gap between the third and fourth bands cannot be illustrated solely by the Zak phase because $\sum_{n=1}^{3} = 2\pi$. Since the Zak phase of 2π is identical to the Zak phase of zero, TESs should not appear. For armchair BPRs, in general, two TES modes appear in the band gap between the third and fourth bands for $\gamma'/\gamma > 1$, in spite of the fact that the Zak phase is 2π. This puzzle is explained by counting the Wannier centers using elementary band representation in the following section.

B. Elementary band representation

In the previous section, we showed that the Zak phase determines the existence of the edge states by numerical calculation. However, the ambiguity about the number of edge states has remained because the Zak phase gives only the

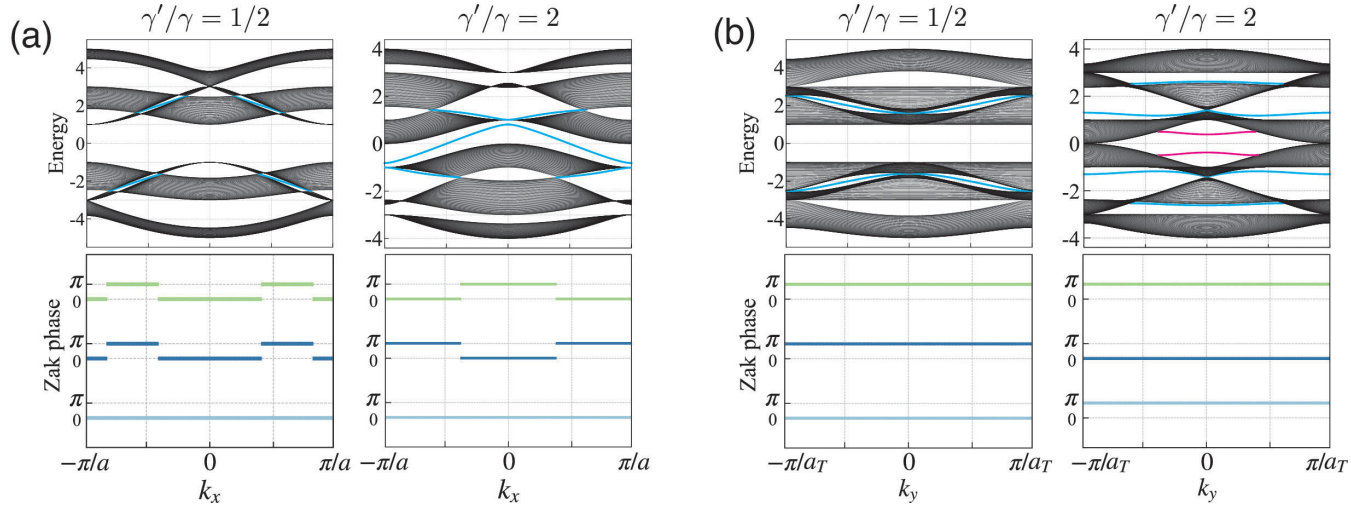

FIG. 5. Energy band structure of the BPR and the corresponding Zak phase. (a) Zigzag BPR with $\gamma'/\gamma = 1/2$ (left) and $\gamma'/\gamma = 2$ (right). In these cases, TESs (cyan lines) emerge in the energy gap where the Zak phase is π. (b) Armchair BPR with $\gamma'/\gamma = 1/2$ (left) and $\gamma'/\gamma = 2$ (right). TESs shown by cyan lines appear in the energy gap where the Zak phase is π. However, TESs shown by magenta lines emerge in the energy band gap where the Zak phase is 2π. The puzzle will be resolved by considering Wannier centers (see the text).

parities of the $\mathbb{Z}_2$ value; for example, the summation of the Zak phase of the occupied bands becomes zero even if there are two edge states in the gap. In order to obtain an accurate number of edge states, we introduce the symmetry analysis using the irreducible representation (irrep) at the high-symmetry points of the first BZ [53–58].

The number of edge states is deeply involved with the central position of the Wannier states (Wannier center) [29,53,59,60]. The edge-terminated line crosses the Wannier orbital n times in a period of the unit cell, and n edge states exist in the gap. The Wannier center is located at the midpoint of the bond with the stronger hopping energy. As discussed before, we considered two types of hopping energies between two atomic sites, i.e., γ and γ'. Here, we identify the position of the Wannier center in terms of the ratio γ'/γ.

To show the relationship between the position of the Wannier center and the stronger hopping bond, we classify the energy bands of the BPN by the irreps of high-symmetry points in the first BZ. The space group of BPN is *Pmmm*, which belongs to point group D_{2h}, and there are eight irreps, as shown in Table I. Here, C_{2j} $(j = x, y, z)$ is the twofold rotation around the j axis, I is the inversion, and σ_j is the mirror reflection with respect to the kl plane $(j, k, l = x, y, z)$.

TABLE I. Character table of point group D_{2h}. The four high-symmetry points in the first BZ belong to the point group D_{2h}.

D_{2h}	E	C_{2z}	C_{2y}	C_{2x}	I	σ_z	σ_y	σ_x
Γ_1^+	1	1	1	1	1	1	1	1
Γ_2^+	1	1	−1	−1	1	1	−1	−1
Γ_3^+	1	−1	1	−1	1	−1	1	−1
Γ_4^+	1	−1	−1	1	1	−1	−1	1
Γ_1^-	1	1	1	1	−1	−1	−1	−1
Γ_2^-	1	1	−1	−1	−1	−1	1	1
Γ_3^-	1	−1	1	−1	−1	1	−1	1
Γ_4^-	1	−1	−1	1	−1	1	1	−1

Each of the six bands in the BPN is classified by the irreps at the high-symmetry points of the first BZ. Since four high-symmetry points in the first BZ have the same symmetry as the BPN lattice, the irreps at the Γ, X, Y, and S points are identical to point group D_{2h}. In Fig. 6, we show the correspondence between the occupied bands of the BPN and the irreps characterized by the symmetry of the wave function. From Fig. 6, we can define the character of the occupied bands by a single vector,

$$\boldsymbol{b} = (\gamma_1^+, \gamma_2^+, \gamma_3^-, \gamma_4^-; x_1^+, x_2^+, x_3^-, x_4^-; \\ y_1^+, y_2^+, y_3^-, y_4^-; s_1^+, s_2^+, s_3^-, s_4^-), \tag{9}$$

where $\gamma_n^\pm$, $x_n^\pm$, $y_n^\pm$, and $s_n^\pm$, with $n = 1, 2, \ldots, 4$, are the numbers of bands whose wave function at the Γ, X, Y, and S points have an irrep $\Gamma_n^\pm$. Here, we omit irreps Γ_3^+, Γ_4^+, Γ_1^-, and Γ_2^-, which are related to the parity with respect to the xy plane, i.e., the symmetry operation of σ_z, because our tight-binding model essentially assumes the s orbital for the atomic orbitals, which always have positive parity with respect to the operation of σ_z and become irrelevant. If we change the atomic orbital on each site from an s orbital to a p_z orbital, we need to take into account irreps Γ_3^+, Γ_4^+, Γ_1^-, and Γ_2^-, but the discussion and the result will not essentially change. Thus,

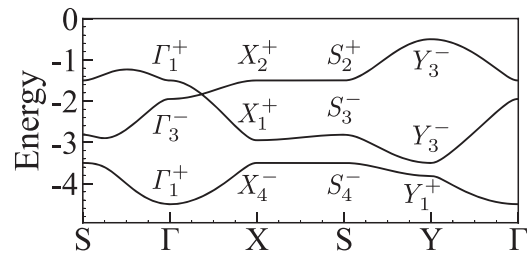

FIG. 6. The irreps of the occupied energy bands for $\gamma' > \gamma$. Note that only the lowest three energy bands of the 2D BPN are displayed.

TABLE II. Elementary band representations of space group *Pmmm*.

WP	SSG	irreps	γ_1^+	γ_2^+	γ_3^-	γ_4^-	x_1^+	x_1^+	x_3^-	x_4^-	y_1^+	y_1^+	y_3^-	y_4^-	s_1^+	s_1^+	s_3^-	s_4^-	η
$1a$ $(0,0)$	*mmm*	Γ_1^+	1	0	0	0	1	0	0	0	1	0	0	0	1	0	0	0	1
		Γ_2^+	0	1	0	0	0	1	0	0	0	1	0	0	0	1	0	0	2
		Γ_3^+	0	0	0	0	0	0	0	0	0	0	0	0	0	0	0	0	3
		Γ_4^+	0	0	0	0	0	0	0	0	0	0	0	0	0	0	0	0	4
		Γ_1^-	0	0	0	0	0	0	0	0	0	0	0	0	0	0	0	0	5
		Γ_2^-	0	0	0	0	0	0	0	0	0	0	0	0	0	0	0	0	6
		Γ_3^-	0	0	1	0	0	0	1	0	0	0	1	0	0	0	1	0	7
		Γ_4^-	0	0	0	1	0	0	0	1	0	0	0	1	0	0	0	1	8
$1b$ $(a,0)$	*mmm*	Γ_1^+	1	0	0	0	0	0	0	1	1	0	0	0	0	0	0	1	9
		Γ_2^+	0	1	0	0	0	0	1	0	0	1	0	0	0	0	1	0	10
		Γ_3^+	0	0	0	0	0	0	0	0	0	0	0	0	0	0	0	0	11
		Γ_4^+	0	0	0	0	0	0	0	0	0	0	0	0	0	0	0	0	12
		Γ_1^-	0	0	0	0	0	0	0	0	0	0	0	0	0	0	0	0	13
		Γ_2^-	0	0	0	0	0	0	0	0	0	0	0	0	0	0	0	0	14
		Γ_3^-	0	0	1	0	0	1	0	0	0	0	1	0	0	1	0	0	15
		Γ_4^-	0	0	0	1	1	0	0	0	0	0	0	1	1	0	0	0	16
$1e$ $(0,a_T)$	*mmm*	Γ_1^+	1	0	0	0	1	0	0	0	0	0	1	0	0	0	1	0	17
		Γ_2^+	0	1	0	0	0	1	0	0	0	0	0	1	0	0	0	1	18
		Γ_3^+	0	0	0	0	0	0	0	0	0	0	0	0	0	0	0	0	19
		Γ_4^+	0	0	0	0	0	0	0	0	0	0	0	0	0	0	0	0	20
		Γ_1^-	0	0	0	0	0	0	0	0	0	0	0	0	0	0	0	0	21
		Γ_2^-	0	0	0	0	0	0	0	0	0	0	0	0	0	0	0	0	22
		Γ_3^-	0	0	1	0	0	0	1	0	1	0	0	0	1	0	0	0	23
		Γ_4^-	0	0	0	1	0	0	0	1	0	1	0	0	0	1	0	0	24
$1f$ (a,a_T)	*mmm*	Γ_1^+	1	0	0	0	0	0	0	1	0	0	1	0	1	0	0	0	25
		Γ_2^+	0	1	0	0	0	0	1	0	0	0	0	1	0	1	0	0	26
		Γ_3^+	0	0	0	0	0	0	0	0	0	0	0	0	0	0	0	0	27
		Γ_4^+	0	0	0	0	0	0	0	0	0	0	0	0	0	0	0	0	28
		Γ_1^-	0	0	0	0	0	0	0	0	0	0	0	0	0	0	0	0	29
		Γ_2^-	0	0	0	0	0	0	0	0	0	0	0	0	0	0	0	0	30
		Γ_3^-	0	0	1	0	0	1	0	0	1	0	0	0	0	0	1	0	31
		Γ_4^-	0	0	0	1	1	0	0	0	0	1	0	0	0	0	0	1	32
$2i$ $(\pm x,0)$	$2mm$	Γ_1	1	0	0	1	1	0	0	1	1	0	0	1	1	0	0	1	33
		Γ_2	0	0	0	0	0	0	0	0	0	0	0	0	0	0	0	0	34
		Γ_3	0	1	1	0	0	1	1	0	0	1	1	0	0	1	1	0	35
		Γ_4	0	0	0	0	0	0	0	0	0	0	0	0	0	0	0	0	36
$2k$ $(\pm x,a_T)$	$2mm$	Γ_1	1	0	0	1	1	0	0	1	0	1	1	0	0	1	1	0	37
		Γ_2	0	0	0	0	0	0	0	0	0	0	0	0	0	0	0	0	38
		Γ_3	0	1	1	0	0	1	1	0	1	0	0	1	1	0	0	1	39
		Γ_4	0	0	0	0	0	0	0	0	0	0	0	0	0	0	0	0	40
$2m$ $(0,\pm y)$	$m2m$	Γ_1	1	0	1	0	1	0	1	0	1	0	1	0	1	0	1	0	41
		Γ_2	0	0	0	0	0	0	0	0	0	0	0	0	0	0	0	0	42
		Γ_3	0	1	0	1	0	1	0	1	0	1	0	1	0	1	0	1	43
		Γ_4	0	0	0	0	0	0	0	0	0	0	0	0	0	0	0	0	44
$2o$ $(a,\pm y)$	$m2m$	Γ_1	1	0	1	0	0	1	0	1	1	0	1	0	0	1	0	1	45
		Γ_2	0	0	0	0	0	0	0	0	0	0	0	0	0	0	0	0	46
		Γ_3	0	1	0	1	1	0	1	0	0	1	0	1	1	0	1	0	47
		Γ_4	0	0	0	0	0	0	0	0	0	0	0	0	0	0	0	0	48
$4y$ $(\pm x,\pm y)$	$..m$	Γ_1	1	1	1	1	1	1	1	1	1	1	1	1	1	1	1	1	49
		Γ_2	0	0	0	0	0	0	0	0	0	0	0	0	0	0	0	0	50
$\boldsymbol{b}_{p_z}$ (occupied p_z bands)			2	0	1	0	1	1	0	1	1	0	2	0	0	1	1	1	$17+45$

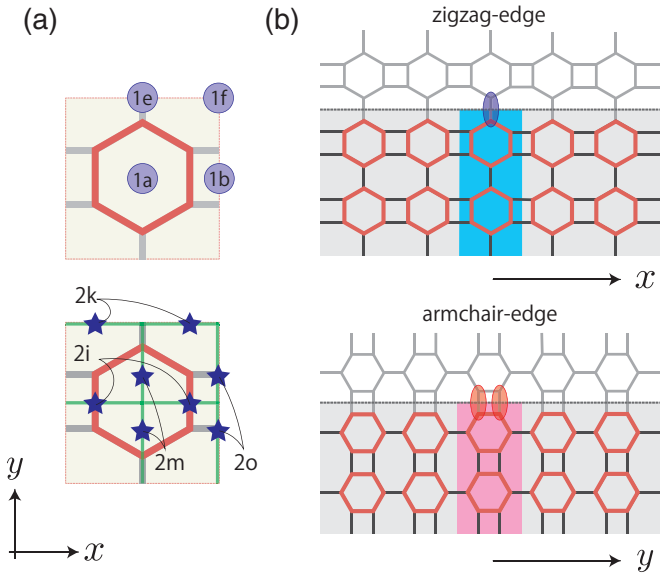

FIG. 7. (a) Wyckoff positions (WPs) on the xy plane for space group *Pmmm*. WPs $2i$, $2k$, $2m$, and $2o$ are two positions on the green lines. In the case of γ' (gray line) $> \gamma$ (red line), the three occupied bands of the BPN consist of two elementary bands, $\boldsymbol{b}_{17}$ (WP $1e$) and $\boldsymbol{b}_{45}$ (WP $2o$) in Table II. (b) Top: Since the edge-terminated line of the zigzag BPR crosses the Wannier orbital (indicated by the blue ellipse) once, one edge state appears. Bottom: On the other hand, the edge-terminated line of the armchair BPR crosses the Wannier orbitals (the red ellipse) twice, which results in two edge states.

the vector of the occupied π bands of the BPN is described as

$$\boldsymbol{b}_{p_z} = (2, 0, 1, 0; 1, 1, 0, 1; 1, 0, 2, 0; 0, 1, 1, 1). \tag{10}$$

Here, we list all elementary bands allowed in space group *Pmmm* in Table II. An elementary band is a set of atomic orbitals situated at the symmetry-protected position, which is called a Wyckoff position (WP). The WP is classified by the site symmetry group (SSG), which guarantees that the WP is invariant in the unit cell. In Fig. 7(a), we show WPs in the unit cell. For instance, eight WPs have the highest symmetry, with the coordinates $1a : (0, 0, 0)$, $1b : (a, 0, 0)$, $1c : (0, 0, z)$, $\ldots$, $1h = (a, a_T, z)$, and their SSGs are identical to the point group of the lattice and have eight irreps. The WPs (and their coordinates) and their corresponding SSGs are shown in the first and second columns of Table II.

Atomic orbitals located at WPs have irreps characterized by SSGs, which are subgroups of the space group of the crystal. Each arrangement of the atomic orbitals is called an elementary band, and the irreps of an elementary band are elementary band representations (EBRs). In Table II, we show all possible EBRs of the WP on xy plane. There are 50 different elementary bands with a serial number η $(= 1, 2, \ldots, 50)$.

In the same manner as in Eq. (9), we shall describe the elementary bands labeled by η as

$$\boldsymbol{b}_\eta = \big(\gamma_1^{+(\eta)}, \gamma_2^{+(\eta)}, \gamma_3^{-(\eta)}, \gamma_4^{-(\eta)}; x_1^{+(\eta)}, x_2^{+(\eta)}, x_3^{-(\eta)}, x_4^{-(\eta)}; y_1^{+(\eta)}, y_2^{+(\eta)}, y_3^{-(\eta)}, y_4^{-(\eta)}; s_1^{+(\eta)}, s_2^{+(\eta)}, s_3^{-(\eta)}, s_4^{-(\eta)}\big). \tag{11}$$

Actual elements of $\boldsymbol{b}_\eta$ are listed in the 4th to 19th columns in Table II, where that Bloch function $e^{i\boldsymbol{k}\cdot\boldsymbol{R}}$ is taken into account

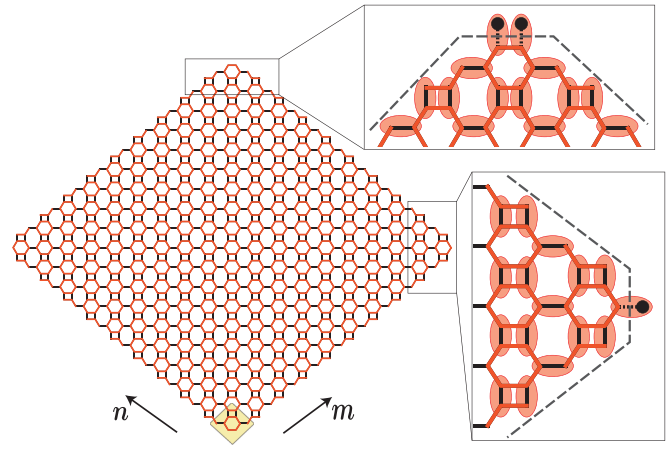

FIG. 8. The structure of the BPN nanoflake for $\gamma' > \gamma$. The red ellipses indicate the Wannier orbitals. Deleting the atom basis indicated by the black dots at the four corners, there are $(m \times n \times 12 - 6)$ atom sites. Wannier orbitals are cut by the corner geometries, resulting in uncoupled Wannier orbitals at the corner sites.

in each character. For example, the EBR of WP $1a$ with $\boldsymbol{R} = (0, 0)$ gives identical irreps among the Γ, X, Y, and S points. In contrast, the EBR of WP $1b$ with $\boldsymbol{R} = (a, 0)$ changes the sequence of the irreducible representations at the X and S points depending on the Bloch phase. The Wannier orbitals are a combination of the elementary bands, and their central positions are the corresponding WPs in the unit cell. As shown in the bottom row of Table II, the Wannier orbitals of the three occupied bands of the BPN can be described as

$$\boldsymbol{b}_{p_z} = \sum_\eta n_\eta \boldsymbol{b}_\eta, \tag{12}$$

where n_η is zero or a positive number. From Table II, n_η is zero except for two EBRs, $\eta = 17$ and $\eta = 45$, whose WPs are $1e$ and $2o$ and which correspond to SSGs *mmm* and *m*2*m*, respectively. Therefore, the occupied bands of the BPN are a linear combination of the two elementary bands $\boldsymbol{b}_{17}$ and $\boldsymbol{b}_{45}$, which are both s-like orbitals situated at WPs $1e$ and $2o$. Hence, the Wannier orbitals are situated at the stronger hopping bonds, and the exact number of edge states can be determined. Figure 7(b) illustrates the broken Wannier orbitals at the zigzag and armchair edge boundaries for $\gamma' > \gamma$. If the strength of the hopping energy is the opposite $(\gamma' < \gamma)$, Wannier orbitals should be situated at the six-member rings (indicated by the red line), not the edge boundaries. Recalling that the 2π Zak phase leads to either zero $(\gamma' < \gamma)$ or two $(\gamma' > \gamma)$ edge states in Sec. III A, it can be understood that the number of broken Wannier orbitals at the edge boundary is consistent with the number of edge states.

C. Topological corner states

In this section, we consider a BPN nanoflake to investigate the conditions for the appearance of topological corner states as "edge-of-edge" states [61–65]. In a manner similar to that in the previous section, we assume a geometry in which the Wannier orbitals are isolated at the boundary of the system. Figure 8 illustrates the structure of the BPN nanoflake formed

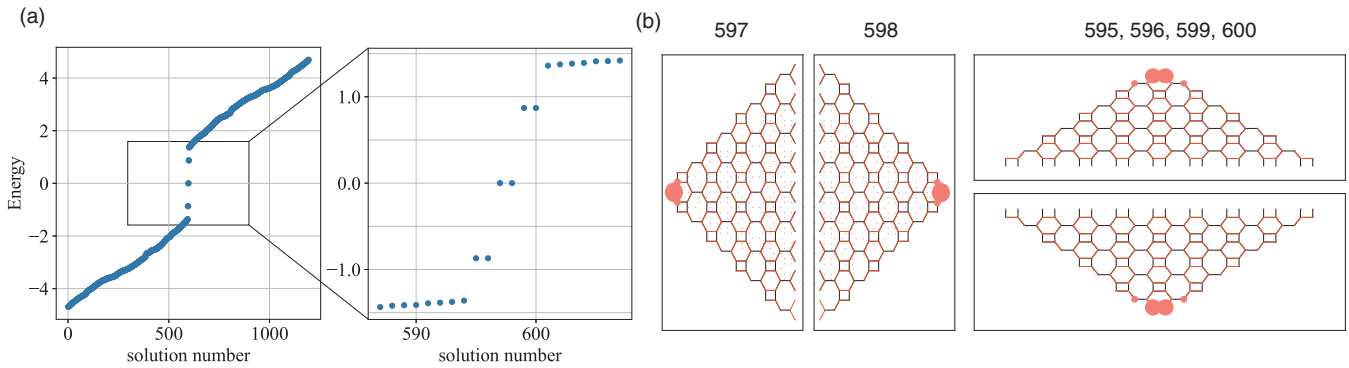

FIG. 9. (a) The energy spectrum of the BPN nanoflake. (b) The amplitude of the wave function of the six energy levels in the gap. Two states are localized in the left and right corners, and the other four states are localized in the upper and lower corners.

by a combination of diagonally cut lines. The rhombus shaded in yellow is a unit which is periodic in the m and n directions. Here, the red lines indicate the hopping of γ, and the black lines indicate the hopping γ'. For $\gamma' > \gamma$, edge states exist in the energy gap, where the Wannier orbitals are located on the bonds indicated by the red ellipses, as shown in the zoom in Fig. 8. Furthermore, if the basis of atomic sites marked by the black circles at the four corners is removed, the Wannier orbitals are broken at the corner sites, i.e., the emergence of corner states.

Figure 9(a) shows the energy spectrum of the nanoflake; the right panel is a zoomed-in view near zero energy. Since the system includes 1194 atoms in the case of $(m, n) = (10, 10)$, the site index has that same number. For $\gamma' > \gamma$, it has an energy gap near zero energy, and six isolated energy levels are found within the gap. Figure 9(b) shows the wave function of the six states within the gap near zero energy. We plot the amplitude of the wave function as the radius of the circles. We can see the exponentially localized states at the corners of the nanoflake. Two states with $E = 0$ are localized in the left and right corners, while the other four states are localized in the lower and upper corners. This can be understood from the positions of the Wannier orbitals. The Wannier orbitals cut by the corner geometry are present: One in the left and right corners and two in the upper and lower corners, resulting in a corresponding number of corner states. Therefore, we can see that these corner states are due to the uncoupled Wannier orbitals at the corners of the system. In addition, changing the values of m and n does not affect the appearance of corner states.

IV. CONCLUSION

In this paper, we have studied the electronic and topological properties of the BPN. We have demonstrated that the BPN exhibits flat bands and tilted Dirac cones, and these tilted cones persist even when the strength of electron hoppings is modified. By varying the ratio of hopping energies, specifically the ratio between intracellular hopping γ and intercellular hopping γ', we can open an energy band gap, leading to a topological phase transition. The emergence of

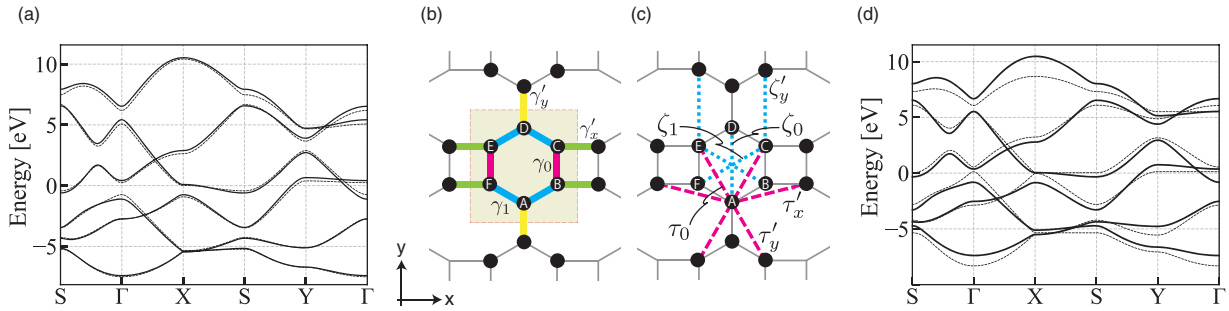

FIG. 10. (a) Energy band structures obtained with DFT (dashed lines) and WANNIER90 (solid lines). In the WANNIER90 calculation, only p_z orbitals of carbon atoms are taken into account for the projection. (b) Schematic of the BPN lattice structure with the definition of nearest-neighbor (NN) hoppings for the tight-binding model of the 2D BPN. The yellow shaded rectangle is the unit cell. γ_0 is the intracellular NN hoppings for the bonds of B-C and E-F. γ_0 is the intracellular NN hoppings for the bonds of A-B, C-D, D-E, and F-A. γ'_x and γ'_y are the intercellular hoppings for the x and y directions, respectively. (c) The definition of second- and third-NN electron hoppings. Magenta thick dashed lines indicate the second-NN hoppings. τ_0 is the intracellular hoppings for the bonds of A-E and A-C. τ'_y is the intercellular hoppings for the bonds of A-E and A-C. τ'_x is the intercellular hoppings for the bonds of A-B and A-F. Cyan dotted lines indicate the third-NN hoppings. ζ_0 is the intracellular hoppings for the bond of A-D. ζ_1 is the intracellular hoppings for the bonds of B-E and C-F. ζ'_y is the intercellular hoppings for the bonds of B-C and E-F. Actual values of the hoppings are summarized in Table III. (d) Energy band structure of the effective tight-binding model considering up to the NN hopping (dashed lines) and the third-NN hopping (solid lines). Inclusion of up to third-NN hoppings reproduces the energy band structures obtained with DFT shown in (a) sufficiently well.

TABLE III. Tight-binding parameters for the 2D BPN. The values are derived from the WANNIER90 calculation. The set of these parameters well reproduces the energy band structures of π electrons for the 2D BPN, as shown in Fig. 10(d). The list of the hopping integrals is given. V_α (V_β) is the on-site potential energy on A and D (B, C, E, and F) sites. The definition of the electron hoppings on the lattice of the 2D BPN are shown in Figs. 10(b) and 10(c).

Potential		NN				Second NN			Third NN		
V_α	V_β	γ_0	γ_1	γ'_x	γ'_y	τ_0	τ'_x	τ'_y	ζ_0	ζ_1	ζ'_y
−2.0742	−2.3647	−2.9603	−2.6910	−2.7479	−2.7962	0.2880	0.3969	0.2473	−0.2041	−0.2991	−0.1920

edge states is guaranteed by a nonzero Zak phase, and the number of edge states aligns with the number of Wannier orbitals at the edge boundary. Using the same principle, we have illustrated the existence of corner states in systems where uncoupled Wannier orbitals are located in the corners. The present theoretical approach is applicable to the design of new materials that share the same structure as BPNs. Although it is very hard to tune the electron hopping energies in actual BPN materials, we can design a system having the topological properties of the BPN based on photonic crystals. The extension to photonic crystals will be discussed elsewhere.

ACKNOWLEDGMENTS

The authors are grateful to M. Hitomi for helpful discussions. This work was supported by JSPS KAKENHI (Grants No. 22H05473, No. JP21H01019, and No. JP18H01154) and JST CREST (Grant No. JPMJCR19T1).

APPENDIX: TIGHT-BINDING PARAMETERS OF 2D BPN

In this Appendix, we present the parameter set for the tight-binding model to describe π-electronic states of the 2D BPN. We implemented first-principles calculations to obtain the energy band structure for the 2D BPN based on the density functional theory (DFT). To this end, we used the QUANTUM ESPRESSO package [66,67] by employing the Perdew-Burke-Ernzerhof variant of the generalized gradient approximation method [68]. A relaxation of the structure was achieved by considering a magnitude of the forces on each atom that is less than 13.6×10^{-4} eV/Å. A $12 \times 14 \times 1$ Monkhorst-Pack mesh [69] was used to sample the first BZ for structural relaxation. Figure 10(a) shows the obtained π-electronic energy band structures of the 2D BPN (dashed lines).

Furthermore, we extracted the tight-binding parameters for π electrons of the 2D BPN using the WANNIER90 package [70]. The parameter set reproduces quite well the energy band structure obtained with DFT, as shown in Fig. 10(a), where the solid lines are the tight-binding calculation obtained with WANNIER90.

Figures 10(b) and 10(c) are schematics for the positions of the hopping integrals for the tight-binding model, where the nearest-neighbor (NN) hoppings are shown in Fig. 10(b). Similarly, the second- and third-NN hoppings are shown in Fig. 10(c). The obtained electron hopping parameters are listed in Table III. Figure 10(d) shows the energy band structure of π electrons for the 2D BPN. The dashed lines indicate the band structure, which includes only NN hoppings. However, the solid lines indicate the energy band structure, which includes up to third-NN hoppings. The inclusion of up to third-NN hoppings reproduces the energy band structure obtained with DFT sufficiently well. Especially, third-NN hoppings are necessary to reproduce the band crossing between the third and fourth subbands on the Y-Γ line, the band gap opening at X, and the slight tilt of the flat band on the X-S line.

[1] C. L. Kane and E. J. Mele, Phys. Rev. Lett. **95**, 226801 (2005).
[2] B. A. Bernevig, T. L. Hughes, and S.-C. Zhang, Science **314**, 1757 (2006).
[3] L. Fu, C. L. Kane, and E. J. Mele, Phys. Rev. Lett. **98**, 106803 (2007).
[4] M. König, S. Wiedmann, C. Brüne, A. Roth, H. Buhmann, L. W. Molenkamp, X.-L. Qi, and S.-C. Zhang, Science **318**, 766 (2007).
[5] M. Z. Hasan and C. L. Kane, Rev. Mod. Phys. **82**, 3045 (2010).
[6] X.-L. Qi and S.-C. Zhang, Rev. Mod. Phys. **83**, 1057 (2011).
[7] D. Hsieh, D. Qian, L. Wray, Y. Xia, Y. S. Hor, R. J. Cava, and M. Z. Hasan, Nature (London) **452**, 970 (2008).
[8] Y. L. Chen, J. G. Analytis, J.-H. Chu, Z. K. Liu, S.-K. Mo, X. L. Qi, H. J. Zhang, D. H. Lu, X. Dai, Z. Fang, S. C. Zhang, I. R. Fisher, Z. Hussain, and Z.-X. Shen, Science **325**, 178 (2009).
[9] C.-Z. Chang *et al.*, Science **340**, 167 (2013).
[10] Y. Ando, J. Phys. Soc. Jpn. **82**, 102001 (2013).
[11] L. Fu, Phys. Rev. Lett. **106**, 106802 (2011).
[12] P. Dziawa, B. J. Kowalski, K. Dybko, R. Buczko, A. Szczerbakow, M. Szot, E. Łusakowska, T. Balasubramanian, B. M. Wojek, M. H. Berntsen, O. Tjernberg, and T. Story, Nat. Mater. **11**, 1023 (2012).
[13] Y. Ando and L. Fu, Annu. Rev. Condens. Matter Phys. **6**, 361 (2015).
[14] X. Wan, A. M. Turner, A. Vishwanath, and S. Y. Savrasov, Phys. Rev. B **83**, 205101 (2011).
[15] A. A. Burkov and L. Balents, Phys. Rev. Lett. **107**, 127205 (2011).
[16] S. Borisenko, Q. Gibson, D. Evtushinsky, V. Zabolotnyy, B. Büchner, and R. J. Cava, Phys. Rev. Lett. **113**, 027603 (2014).
[17] Q.-F. Liang, J. Zhou, R. Yu, Z. Wang, and H. Weng, Phys. Rev. B **93**, 085427 (2016).

[18] H. Watanabe, H. C. Po, M. P. Zaletel, and A. Vishwanath, Phys. Rev. Lett. **117**, 096404 (2016).
[19] B.-J. Yang, T. A. Bojesen, T. Morimoto, and A. Furusaki, Phys. Rev. B **95**, 075135 (2017).
[20] S. Raghu and F. D. M. Haldane, Phys. Rev. A **78**, 033834 (2008).
[21] Z. Wang, Y. D. Chong, J. D. Joannopoulos, and M. Soljačić, Phys. Rev. Lett. **100**, 013905 (2008).
[22] A. B. Khanikaev, S. H. Mousavi, W. K. Tse, M. Kargarian, A. H. MacDonald, and G. Shvets, Nat. Mater. **12**, 233 (2013).
[23] L. Lu, J. Joannopoulos, and M. Soljačić, Nat. Photon. **8**, 821 (2014).
[24] Y. Liu, X. Chen, and Y. Xu, Adv. Func. Mater. **30**, 1904784 (2020).
[25] C. Lee, S. Imhof, C. Berger, F. Bayer, J. Brehm, L. W. Molenkamp, T. Kiessling, and R. Thomale, Commun. Phys. **1**, 39 (2018).
[26] J. Zak, Phys. Rev. Lett. **62**, 2747 (1989).
[27] R. D. King-Smith and D. Vanderbilt, Phys. Rev. B **47**, 1651 (1993).
[28] R. Resta, Rev. Mod. Phys. **66**, 899 (1994).
[29] N. Marzari, A. A. Mostofi, J. R. Yates, I. Souza, and D. Vanderbilt, Rev. Mod. Phys. **84**, 1419 (2012).
[30] Y. Zhou, K. M. Rabe, and D. Vanderbilt, Phys. Rev. B **92**, 041102(R) (2015).
[31] F. Liu and K. Wakabayashi, Phys. Rev. Lett. **118**, 076803 (2017).
[32] M. Fujita, K. Wakabayashi, K. Nakada, and K. Kusakabe, J. Phys. Soc. Jpn. **65**, 1920 (1996).
[33] K. Nakada, M. Fujita, G. Dresselhaus, and M. S. Dresselhaus, Phys. Rev. B **54**, 17954 (1996).
[34] K. Wakabayashi, M. Fujita, H. Ajiki, and M. Sigrist, Phys. Rev. B **59**, 8271 (1999).
[35] S. Ryu and Y. Hatsugai, Phys. Rev. Lett. **89**, 077002 (2002).
[36] P. Delplace, D. Ullmo, and G. Montambaux, Phys. Rev. B **84**, 195452 (2011).
[37] K. Wakabayashi, Y. Takane, M. Yamamoto, and M. Sigrist, Carbon **47**, 124 (2009).
[38] K. Wakabayashi, S. Okada, R. Tomita, S. Fujimoto, and Y. Natsume, J. Phys. Soc. Jpn. **79**, 034706 (2010).
[39] Y.-W. Son, M. L. Cohen, and S. G. Louie, Phys. Rev. Lett. **97**, 216803 (2006).
[40] K. Wakabayashi, Y. Takane, and M. Sigrist, Phys. Rev. Lett. **99**, 036601 (2007).
[41] Q. Fan, L. Yan, M. W. Tripp, O. Krejčí, S. Dimosthenous, S. R. Kachel, M. Chen, A. S. Foster, U. Koert, P. Liljeroth, and J. M. Gottfried, Science **372**, 852 (2021).
[42] A. Bafekry, M. Faraji, M. M. Fadlallah, H. R. Jappor, S. Karbasizadeh, M. Ghergherehchi, and D. Gogova, J. Phys.: Condens. Matter **34**, 015001 (2022).
[43] Y. Luo, C. Ren, Y. Xu, J. Yu, S. Wang, and M. Sun, Sci. Rep. **11**, 19008 (2021).
[44] Y. W. Son, H. Jin, and S. Kim, Nano Lett. **22**, 3112 (2022).
[45] L.-J. Ma, Y. Sun, J. Jia, and H.-S. Wu, Fuel **357**, 129652 (2024).
[46] W. P. Su, J. R. Schrieffer, and A. J. Heeger, Phys. Rev. B **22**, 2099 (1980).
[47] A. J. Heeger, S. Kivelson, J. R. Schrieffer, and W. P. Su, Rev. Mod. Phys. **60**, 781 (1988).
[48] F. Liu, M. Yamamoto, and K. Wakabayashi, J. Phys. Soc. Jpn. **86**, 123707 (2017).
[49] D. Obana, F. Liu, and K. Wakabayashi, Phys. Rev. B **100**, 075437 (2019).
[50] S. S. Pershoguba and V. M. Yakovenko, Phys. Rev. B **86**, 075304 (2012).
[51] T. Kameda, F. Liu, S. Dutta, and K. Wakabayashi, Phys. Rev. B **99**, 075426 (2019).
[52] T. Fukui, Y. Hatsugai, and H. Suzuki, J. Phys. Soc. Jpn. **74**, 1674 (2005).
[53] J. Kruthoff, J. de Boer, J. van Wezel, C. L. Kane, and R.-J. Slager, Phys. Rev. X **7**, 041069 (2017).
[54] B. Bradlyn, L. Elcoro, J. Cano, M. G. Vergniory, Z. Wang, C. Felser, M. I. Aroyo, and B. A. Bernevig, Nature (London) **547**, 298 (2017).
[55] J. Cano, B. Bradlyn, Z. Wang, L. Elcoro, M. G. Vergniory, C. Felser, M. I. Aroyo, and B. A. Bernevig, Phys. Rev. B **97**, 035139 (2018).
[56] J. Cano and B. Bradlyn, Annu. Rev. Condens. Matter Phys. **12**, 225 (2020).
[57] M. Hitomi, T. Kawakami, and M. Koshino, Phys. Rev. B **104**, 125302 (2021).
[58] T. Tani, M. Hitomi, T. Kawakami, and M. Koshino, Phys. Rev. B **105**, 075407 (2022).
[59] Z. Song, Z. Fang, and C. Fang, Phys. Rev. Lett. **119**, 246402 (2017).
[60] Y. Xu, L. Elcoro, Z.-D. Song, M. G. Vergniory, C. Felser, S. S. P. Parkin, N. Regnault, J. L. Mañes, and B. A. Bernevig, arXiv:2106.10276.
[61] J. Langbehn, Y. Peng, L. Trifunovic, F. von Oppen, and P. W. Brouwer, Phys. Rev. Lett. **119**, 246401 (2017).
[62] K. Hashimoto, X. Wu, and T. Kimura, Phys. Rev. B **95**, 165443 (2017).
[63] M. Ezawa, Phys. Rev. Lett. **120**, 026801 (2018).
[64] W. A. Benalcazar, B. A. Bernevig, and T. L. Hughes, Science **357**, 61 (2017).
[65] F. Liu and K. Wakabayashi, Phys. Rev. Res. **3**, 023121 (2021).
[66] P. Giannozzi *et al.*, J. Phys.: Condens. Matter **21**, 395502 (2009).
[67] P. Giannozzi *et al.*, J. Phys.: Condens. Matter **29**, 465901 (2017).
[68] J. P. Perdew, K. Burke, and M. Ernzerhof, Phys. Rev. Lett. **77**, 3865 (1996).
[69] H. J. Monkhorst and J. D. Pack, Phys. Rev. B **13**, 5188 (1976).
[70] A. A. Mostofi, J. R. Yates, G. Pizzi, Y.-S. Lee, I. Souza, D. Vanderbilt, and N. Marzari, Comput. Phys. Commun. **185**, 2309 (2014).